Received: 28 January 2020 | Revised: 2 April 2020 | Accepted: 3 April 2020

DOI: 10.1002/eng2.12177

SHORT COMMUNICATION

WILEY

Hybrid datasets: Incorporating experimental data into Lattice-Boltzmann simulations

Helen E. Morrison[1,2] | **Andreas Lintermann**[3,4] | **Sven Grundmann**[1]

[1]Chair of Fluid Mechanics, University of Rostock, Rostock, Germany

[2]Chair of Ocean Engineering, University of Rostock, Justus-von-Liebig-Weg 2, Rostock, 18059, Germany

[3]Jülich Supercomputing Centre, Forschungszentrum Jülich GmbH, Jülich, Germany

[4]JARA Center for Simulation and Data Science, RWTH Aachen University and Forschungszentrum Jülich GmbH, Aachen and Jülich, Germany

Correspondence
Sven Grundmann, Chair of Fluid Mechanics, University of Rostock, Justus-von-Liebig-Weg 2, Rostock 18059, Germany.
Email: sven.grundmann@uni-rostock.de

Summary

A novel method, which combines both fluid-mechanical experimental and numerical data from magnetic resonance velocimetry and Lattice-Boltzmann (LB) simulations is presented. The LB method offers a unique and simple way of integrating the experimental data into the simulation by means of its equilibrium term. The simulation is guided by the experimental data, while at the same time potential outliers or noisy data are physically smoothed. In addition, the simulation allows to increase the resolution and to obtain further physical quantities, which are not measurable in the experiment. For a benchmark case, temporally averaged velocity data is included into the simulation. The proposed model creates a hybrid dataset, which satisfies the Reynolds-averaged Navier-Stokes equations, including the correctly deduced contribution from the Reynolds stress tensor.

KEYWORDS

Lattice-Boltzmann method, hybrid simulation, magnetic resonance velocimetry, Reynolds-averaged Navier-Stokes equations

1 | INTRODUCTION

In fluid dynamics, experiments, and simulations are frequently conducted independently from one another. While experiments aim at analyzing an existing flow field in as much detail as possible and with the highest realizable accuracy, simulations aim at reproducing the corresponding flow field. Experiments are frequently used to validate numerical results. In turn, simulations may offer higher spatial and temporal resolutions and ideally more details on the evolving flow. However, such simulations require accurate boundary conditions and rely on turbulence modeling whenever a direct numerical simulation (DNS) is not feasible. In case the simulation approach does not fully satisfy the physical constraints, the simulation results may considerably differ from reality and consequently also from the experimental data.

Several approaches, which combine experimental data with (hydrodynamic) models, have been introduced in the literature. They enable a better predictability of the models on the one hand and a physical filtering of experimental data on the other hand. These approaches are most commonly summarized under the term *data assimilation*.[1] They are especially popular in meteorology and geophysics, where they are used to obtain precise forecast models.[2,3] Data assimilation has also been used in the context of the Navier-Stokes equations, where experimental data is often combined

with the underlying equations in order to solve optimization problems.[4] Furthermore, Suzuki et al.[5] introduced the term *hybrid simulation*. In their method, time-resolved particle tracking velocimetry data are directly incorporated into DNS simulations. This can generally be done via several different approaches, which vary mainly by the complexity of the feedback mechanism.[6] Hybrid datasets can furthermore be obtained from proper orthogonal decomposition (POD) modes in the context of the Galerkin projection of the Navier-Stokes equations.[7,8] Continuous feedback can be used to physically smooth experimental data and to estimate the temporal development of the POD modes. Romain et al.[9] and Suzuki[10] use Kalman filters to integrate temporally resolved particle image velocimetry (PIV) data into reduced-order models based on POD modes and DNS simulations of the Navier-Stokes equations, respectively. The corresponding feedback mechanism thereby takes spatial and temporal correlations into account, which allows to obtain hybrid datasets of high REYNOLDS number flows, even when the experimental data is noisy. The disadvantages of this method are its high memory and computational requirements.[6]

In general though, the existing approaches focus on (i) time-resolved experimental data, which are frequently only available in two-dimensional slices, and (ii) external flows, which are optically accessible using suitable measuring techniques. By contrast to the aforementioned methods, the magnetic resonance velocimetry (MRV) enables the measurement of fully three-dimensional velocity datasets of arbitrarily complex flows.[11,12] In most cases, these datasets are spatially highly resolved but also temporally averaged, that is, they do not necessarily fulfill the Navier-Stokes equations, but the Reynolds-averaged Navier-Stokes (RANS) equations. From a numerical point of view, Lattice-Boltzmann (LB) methods have proven to be a valuable tool for the simulation of complex flows in complex geometries.[13-15] Boundary conditions can readily be prescribed, the explicit formulation of the discretized LB equations allows for efficient parallelization and computation, and meshing can be performed fully automatically. First coupled MRV-LB simulations have been presented by Klemens et al.,[16] which use the parameterized Bhatnagar-Gross-Krook (BGK) equation for porous media to identify solid bodies in flow fields. Therefore, a distributed control problem for the minimization between the MRV data and the LB results is solved using an adjoint method. An adjoint method for the adaptation of numerical to experimental results is furthermore proposed in Lemke et al.[17] One- and two-dimensional laminar flame configurations are analyzed by means of variational data assimilation techniques. The adjoint is used to iteratively reduce the gradient of the target function, which needs to be minimized regarding the differences between simulation and experiment. This method is also employed by Lemke and Sesterhenn[18] and Gray et al.[19] In Lemke and Sesterhenn,[18] the difference between PIV measurements and simulation results is determined to obtain the pressure distribution. The analyses in Gray et al.[19] focus on the transition from deflagration to detonation in a detonation-shock chamber, for which experimental pressure values are available. A simulation of the one-dimensional reactive Navier-Stokes equations is adapted to the experiments. The method is steered with the help of the Arrhenius parameter and the diffusion coefficients.

In the following, a novel method is presented to create hybrid datasets by incorporating experimental temporally averaged MRV data into LB simulations with the aim of generating datasets that generally obey the RANS equations. These hybrid datasets are guided by a steering parameter that determines how much a simulation is guided by the experimental input. The results of the experiments, the pure LB simulation, and the hybrid approach are juxtaposed for the turbulent flow in the wake of a bluff body.

The details on the methodology of the hybrid method are presented in Section 2. Subsequently, this method is applied to generate a hybrid dataset in Section 3, before some conclusions are drawn in Section 4.

2 | HYBRID SIMULATIONS USING AN LB METHOD

In this study, hybrid datasets are obtained by combining MRV datasets with an LB method. The latter has become an increasingly popular method for the simulation of hydrodynamic problems. Unlike "traditional" computational fluid dynamics methods, which solve the Navier-Stokes equations by, for example, finite-volume, -element, or -differences methods, the LB method solves the discretized LB equation, that is,

$$f_i(\boldsymbol{x} + \boldsymbol{c}_i, t + 1) = \Omega_i + f_i(\boldsymbol{x}, t), \tag{1}$$

where $f_i(\boldsymbol{x}, t), i = 0, \ldots, q - 1$ are particle probability distribution functions (PPDFs) at position $\boldsymbol{x}$ and time t. The vectors $\boldsymbol{c}_i$ represent the respective discretized velocity vectors on a uniform lattice and Ω_i is a collision term. Two-dimensional lattices frequently use $q = 9$ directions, that is, the so-called D2Q9 discretization scheme.[20] In three dimensions, the

D3Q19 or D3Q27 schemes are commonly employed. The macroscopic variables such as the density ρ or the momentum $\rho\boldsymbol{u}$ can be computed from the corresponding moments of the PPDFs, i.e., $\{\rho, \rho\boldsymbol{u}\} = \sum_{i=0}^{q-1}\{1, \boldsymbol{c}_i\}f_i$. The left- and right-hand sides of Equation (1) correspond to a streaming and collision step, respectively.

The lattice-BGK model[21] implements the simplest form of the collision term Ω_i by introducing a single-relaxation-time (SRT). In this case, the PPDFs are relaxed toward their local equilibrium f_i^{eq} with a relaxation time τ. Then, Equation (1) becomes

$$f_i(\boldsymbol{x} + \boldsymbol{c}_i, t+1) = \frac{1}{\tau}\left[f_i^{eq}(\boldsymbol{x}, t) - f_i(\boldsymbol{x}, t)\right] + f_i(\boldsymbol{x}, t). \tag{2}$$

The equilibrium term f_i^{eq} is given by the Maxwell-Boltzmann distribution, which for small MACH numbers $Ma = |\boldsymbol{u}|/c_s \ll 1$ can be expanded up to second order in the fluid velocity $\boldsymbol{u}$ to yield

$$f_i^{eq}(\boldsymbol{x}, t) = \rho t_i \left[1 + \frac{(\boldsymbol{c}_i \cdot \boldsymbol{u})}{c_s^2} + \frac{(\boldsymbol{c}_i \cdot \boldsymbol{u})^2 - c_s^2(\boldsymbol{u} \cdot \boldsymbol{u})}{2c_s^4}\right]. \tag{3}$$

In this equation, c_s is the speed of sound in lattice units and t_i are lattice specific constants. From Equations (2) and (3), the Navier-Stokes equations can be recovered via the Chapman-Enskog expansion, which also results in an expressions for the pressure P and the kinematic viscosity ν, that is, $P = \rho c_s^2$ and $\nu = c_s^2(\tau - 1/2)$.

It should thus be noted that the collision term is a function of the viscosity ν and hence also of the REYNOLDS number Re. For $Re \to \infty$, $\nu \to 0$ and subsequently $1/\tau \to 2$, which represents the upper stability limit of the SRT method. Despite its simple nature, the SRT method is able to produce satisfactory results as long as the considered MACH number is chosen to represent quasi-incompressible flow, the REYNOLDS number is low, and the resolution is sufficient. The limitation to the MACH number is inherently given by the Taylor series expansion, which relies on small MACH numbers to obtain Equation (3). The REYNOLDS number determines the size of turbulent scales, that is, with increasing REYNOLDS numbers higher mesh resolutions are required to capture all relevant flow features. Nathen et al.[22] performed investigations on the impact of the mesh resolution on the stability of the BGK method. They found that stable results are obtained, if the flow scales are sufficiently resolved. By contrast, if the turbulent flow scales are not sufficiently resolved, nonlinear instabilities develop, which is also in agreement with other findings.[23] For hybrid simulations, the aim is to keep the resolution as low as possible, while using the experimental data to guide the simulation toward a plausible result. To avoid stability issues, the so-called entropic multirelaxation time (MRT) LB method, or KBC model,[24,25] is used. In this model, the PPDFs are divided into a kinetic part k_i and a part which contains the shear stress s_i and higher order terms h_i: $f_i = k_i + s_i + h_i$. The collision term Ω_i then becomes

$$\Omega_i = \frac{1}{\tau}\left[\left(s_i^{eq} - s_i\right) + \frac{\gamma}{2}\left(h_i^{eq} - h_i\right)\right], \tag{4}$$

where s_i^{eq} and h_i^{eq} are obtained from f_i^{eq}, and γ is an additional relaxation time for the higher order moments, which enables unconditional numerical stability. Further moment-based methods, which could in principle also be used for the proposed hybrid simulations, include the pure MRT[26,27] and the cascaded LB (CLB)[27,28] methods. The MRT decouples the conservative from the nonconservative variables by using multiple relaxation times in moment space leading to higher accuracy and stability. The two-relaxation-time (TRT)[29] model represents a subset of the MRT methods and introduces TRTs, that is, one each for even and odd order tensors. In the CLB method, moments up to fourth order are reconstructed from lower order moments in a cascade to accurately capture oscillations of short wavelengths. A further collision model is given by the regularized LB method,[30] which splits the collision operator into equilibrium and nonequilibrium parts. Using nonequilibrium shears, the collision term is then transformed into a solvable form. Furthermore, the cumulant LB method[31] introduces a collision operator based on the so-called cumulants and has shown good performance for high REYNOLDS number flows. The stability of all these various methods can be analyzed by performing a Fourier transformation of the system of equations under the assumption of a linearized equilibrium term and then investigating the eigenvalues of the iteration matrix in spectral space.[23] For a more detailed review of LB methods the reader is referred to Aidun and Clausen.[32]

The local equilibrium term, which is present in all collision models, offers a unique opportunity to incorporate experimental velocity data. It requires a recomputation of the local density and velocity at each iteration in each individual computational cell from the respective PPDFs. Instead of using the computed velocity from the LB simulation $\boldsymbol{u}^{\mathrm{LBM}}$, either

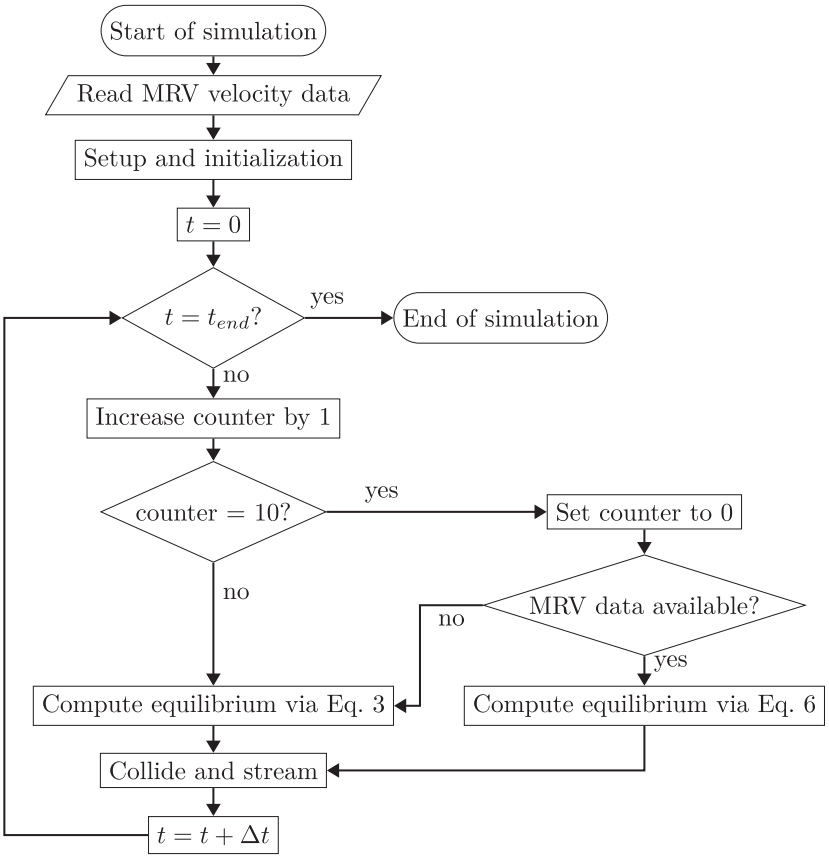

FIGURE 1 Flow chart of the hybrid simulations

the measured velocity $\boldsymbol{u}^{\mathrm{EXP}}$ or a blended combination of both

$$\begin{aligned}\tilde{\boldsymbol{u}} &= (1-\lambda)\left[\frac{1}{\rho}\sum_{i=0}^{q-1}\boldsymbol{c}_i f_i(\boldsymbol{x},t)\right] + \lambda\boldsymbol{u}^{\mathrm{EXP}} \\ &= (1-\lambda)\boldsymbol{u}^{\mathrm{LBM}} + \lambda\boldsymbol{u}^{\mathrm{EXP}},\end{aligned} \tag{5}$$

can be used. The quantity $\lambda \in [0,1]$ is a factor, which dictates to which percentage the measured velocity should be used compared with the simulated velocity. The Maxwellian equilibrium function with the updated blended velocity then reads

$$f_i^{eq}(\boldsymbol{x},t) = \rho t_i\left[1 + \frac{(\boldsymbol{c}_i\cdot\tilde{\boldsymbol{u}})}{c_s^2} + \frac{(\boldsymbol{c}_i\cdot\tilde{\boldsymbol{u}})^2 - c_s^2(\tilde{\boldsymbol{u}}\cdot\tilde{\boldsymbol{u}})}{2c_s^4}\right]. \tag{6}$$

Using this method results in a hybrid dataset. To obtain the results presented in Section 3, the equilibrium term is updated every 10 LB iterations at every position $\boldsymbol{x}$, where experimental velocity data is available. A flow chart of the hybrid simulations, focusing on the incorporation of the experimental data, is shown in Figure 1.

The blending factor λ is assumed to be constant in space and time. Note that λ could also be chosen to depend on the reliability of the respective experimental data. All simulations are run using an extended version of the open-source Palabos library.[1]

3 | FLOW IN THE WAKE OF A BLUFF BODY

To benchmark the proposed approach, a case by Elkins et al.,[33] which is similar to the backward facing step in a channel flow, is chosen. Elkins et al. conducted both MRV and PIV experiments for this case. The MRV measurements were subsequently repeated by Freudenhammer et al.,[34] thus providing the authors of this article with a full three-dimensional

[1]https://palabos.unige.ch/

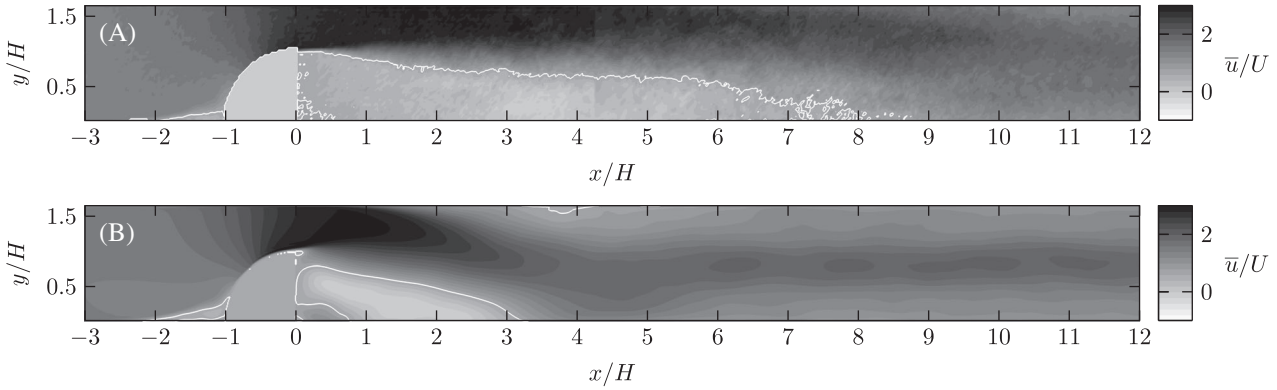

FIGURE 2 Time-averaged horizontal velocity component as, A, measured with MRV, B, obtained from the two-dimensional LB simulation with $\lambda = 0$. LB, Lattice-Boltzmann; MRV, magnetic resonance velocimetry

MRV dataset. The benchmark considers a wall-mounted bluff body in the shape of quarter of a circular cylinder with a radius of $H = 30$mm. The rounded side of the body faces upstream and the cylinder covers the entire width of the square channel. The channel has a width and height of $\Delta y = \Delta z = 50$mm and is $\Delta x = 550$mm long. At the inlet, 100mm upstream of the body, a block velocity profile with a free-stream velocity of $U^{\mathrm{EXP}} = 0.41$m/s is generated. The chosen fluid for the flow is water. The REYNOLDS number of the problem is $Re^{\mathrm{EXP}} = U^{\mathrm{EXP}}H/\nu = 12,300$, which results in an unsteady flow downstream of the body. The resolution of the available dataset corresponds to approximately $N^{\mathrm{EXP}} = 30$ data points per body height. Figure 2A shows the time-averaged MRV velocity component in x-direction normalized by the free-stream velocity $\overline{u}/U$. As expected, a recirculation zone, which extends up to $x/H \sim 8$, exists behind the body.

The benchmark is initially simulated with a two-dimensional LB method without incorporating the experimental MRV data, that is, using $\lambda = 0$. The simulation is run at the same REYNOLDS number as in the experiments, namely, $Re^{\mathrm{LBM}} = U^{\mathrm{LBM}}H/\nu = Re^{\mathrm{EXP}} = 12{,}300$. The resolution is $N^{\mathrm{LBM}} = 100$ cells per body height. With the bottom right corner of the bluff body placed at $x/H = 0$ and $y/H = 0$, the simulation domain extends over $-3.5 \leq x/H \leq 18.5$ in the horizontal direction and $0 \leq y/H \leq 1.67$ in the vertical direction, resulting in a total of 310,968 cells. The inlet boundary is placed at $x/H = -3.5$, where the boundary velocity u_b is given by the lattice velocity $u_b = U^{\mathrm{LBM}}$, such that the flow is in positive x-direction. The lattice velocity itself is set to $U^{\mathrm{LBM}} = 0.01$, so as to also allow for considerably larger local velocities, which are particularly to be expected directly above and behind the bluff body. At the upper and lower boundaries at $y/H = 0$ and $y/H = 1.67$, respectively, no-slip wall boundary conditions are prescribed. For numerical stability, the velocity boundaries employ the Tamm-Mott-Smith (TMS) approximation.[35] Following this approach, the PPDFs at the boundaries are computed by using a combination of the known PPDFs and a target velocity and density, u_{tgt} and ρ_{tgt}, with the missing PPDFs denoted as a subset $f_i, i \in \overline{D}$:

$$f_i = \begin{cases} 2f_i^{eq}(\rho_{tgt}, \boldsymbol{u}_{tgt}) - f_i^{eq}(\rho^*, \boldsymbol{u}^*), & i \in \overline{D} \\ f_i + f_i^{eq}(\rho_{tgt}, \boldsymbol{u}_{tgt}) - f_i^{eq}(\rho^*, \boldsymbol{u}^*), & i \notin \overline{D} \end{cases} \tag{7}$$

with

$$\rho^* = \sum_{i \in \overline{D}} f_i^{eq}(\rho_{tgt}, \boldsymbol{u}_{tgt}) + \sum_{i \notin \overline{D}} f_i \tag{8}$$

$$\boldsymbol{u}^* = \frac{1}{\rho^*}\left(\sum_{i \in \overline{D}} f_i^{eq}(\rho_{tgt}, \boldsymbol{u}_{tgt})\boldsymbol{c}_i + \sum_{i \notin \overline{D}} f_i \boldsymbol{c}_i\right). \tag{9}$$

For velocity boundaries, the target velocity is given by the specified boundary velocity $u_{tgt} = u_b$. The target density can then be computed by[36] $\rho_{tgt} = (2f_+ + f_b)/(1 + u_b)$, where f_+ is the sum of all PPDFs pointing out of the domain and f_b is the sum of the PPDFs on the boundary. The outflow boundary at $x/H = 18.5$ uses the approach described by Chikatamarla et al.[37] The bluff body is treated using a combination of the interpolated bounce-back scheme from

Bouzidi et al.[38] and the TMS approximation, as previously used by Morrison and Leder.[39] The required wall distances are calculated analytically.

Figure 2B shows the time-averaged x-velocity component from the simulation after 10^6 LB iterations. Clearly, the resulting recirculation zone behind the body is much shorter compared with the MRV measurement results, cf. Figure 2A. It extends to only $x/H \sim 3.2$. This is most likely due to the missing influence of the lateral walls and the fact that no three-dimensional effects can be captured with a two-dimensional simulation. From the results it is clear that the benchmark is three-dimensional by nature. It is precisely the large error of the simulation though, which makes it the ideal case for the proposed hybrid simulation method. The idea is that by adding information from the measurements, the simulation will be "nudged" toward the desired solution, while still providing a good solution of the RANS equation.

It is worth pointing out that the test case could in fact also be simulated with a fully three-dimensional LB simulation. With correct boundary conditions and sufficient accuracy, this simulation would also provide the correct flow around the bluff body. While this would clearly increase the computational costs of the simulation, the proposed novel approach does not primarily aim at reducing the run time needed to obtain a correct dataset. Instead it can be used to avoid complex boundary conditions, for example, regarding an accurate velocity profile at the inlet, and the need for large resolutions when simulating turbulent flows. At the same time, potentially noisy experimental data can be corrected and the dataset can be extended by the simulation, for example, in the vicinity of boundaries, which cannot always be sufficiently captured by the experiments. Nevertheless, obtaining such an experimental dataset is also relatively time-consuming and may even outweigh the reduced computational costs between a carefully constructed LB simulation and a hybrid simulation in some cases.

In order to incorporate the MRV data, the measured velocities are first interpolated onto the LB lattice using tri-linear interpolation. No further filtering or manipulation of the measurement data is introduced, that is, potential outliers and noise resulting from measurement uncertainties are still contained. The objective is to show that the method presented in Section 2 is able to create hybrid datasets, which allow to reconstruct MRV data while simultaneously applying a physical smoothing to eliminate potential outliers.

The time-averaged MRV data is incorporated into the simulation using Equation (5) and an arbitrarily fixed λ. Although the equilibrium PPDFs are calculated in each cell at each LB iteration, the velocity $\tilde{\boldsymbol{u}}$ is updated using the MRV data only every 10 LB iterations. In all intermediate iterations, the LB method is allowed to evolve without modification. Furthermore, the MRV data is only integrated into cells where data is available from the lattice interpolation. The simulation setup itself remains identical to the pure LB case outlined above.

Using this method, the simulation should ideally be guided toward a solution that, when averaged over time, is governed by the RANS equations, which read

$$\overline{u}_j \frac{\partial \overline{u}_i}{\partial x_j} + \frac{1}{\rho}\frac{\partial \overline{P}}{\partial x_i} - \nu \frac{\partial^2 \overline{u}_i}{\partial x_j^2} = -\frac{\partial R_{ij}}{\partial x_j}\boldsymbol{e}_i. \tag{10}$$

In this equation, the Einstein summation convention is used. The quantities $\overline{u}_i$ are the time-averaged velocity vector components, $\overline{P}$ is the time-averaged pressure, $R_{ij} = \overline{u_i' u_j'}$ are the components of the Reynolds stress tensor $\boldsymbol{R}$, and $\boldsymbol{e}_i$ is the respective unit vector. The right-hand side is effectively the divergence of the Reynolds stress tensor (div($\boldsymbol{R}$)). Furthermore, all terms on the left-hand side of Equation (10) can be determined by computing the corresponding macroscopic fluid variables from the PPDFs, with $\overline{\boldsymbol{u}}$ and $\overline{P} = \overline{\rho} c_s^2$ being updated at every LB iteration. The respective gradients are determined in a postprocessing step. That is, if the hybrid simulation is able to reproduce the time average of the fully turbulent flow as measured by the MRV, the divergence of the Reynolds stress tensor can be calculated by Equation (10) when all left-hand side terms are determined by the results of the hybrid simulation.

Figure 3 depicts the contours of the left-hand side terms for several hybrid simulations with varying $\lambda \in \{0, 1 \cdot 10^{-4}, 5 \cdot 10^{-4}, 1 \cdot 10^{-3}, 1 \cdot 10^{-2}\}$. From these results it is obvious that the larger λ, the more the simulation is forced toward the incorporated experimental data. The bottom image shows the Reynolds stress term values calculated from experimental data obtained with laser Doppler anemometry (LDA). The Reynolds stress term has low values in the area upstream of the body and has two distinct areas of higher values at the edges of the shear layer. The top image of Figure 3 shows the simulation results without any influence of the experimental data. The contour plot features large values across large areas downstream of the bluff body. When compared with the LDA results, it becomes clear that in this case the computed flow is far from a physically meaningful turbulent flow. Obviously, the right-hand side of Equation (10), i.e., the Reynolds stress term, dominates the whole equation. The images below show the simulation results with increasing λ and hence an increasing influence of the experimental data is visible. Already for low values of λ, that is, $\lambda = 5 \cdot 10^{-4}$, the overall

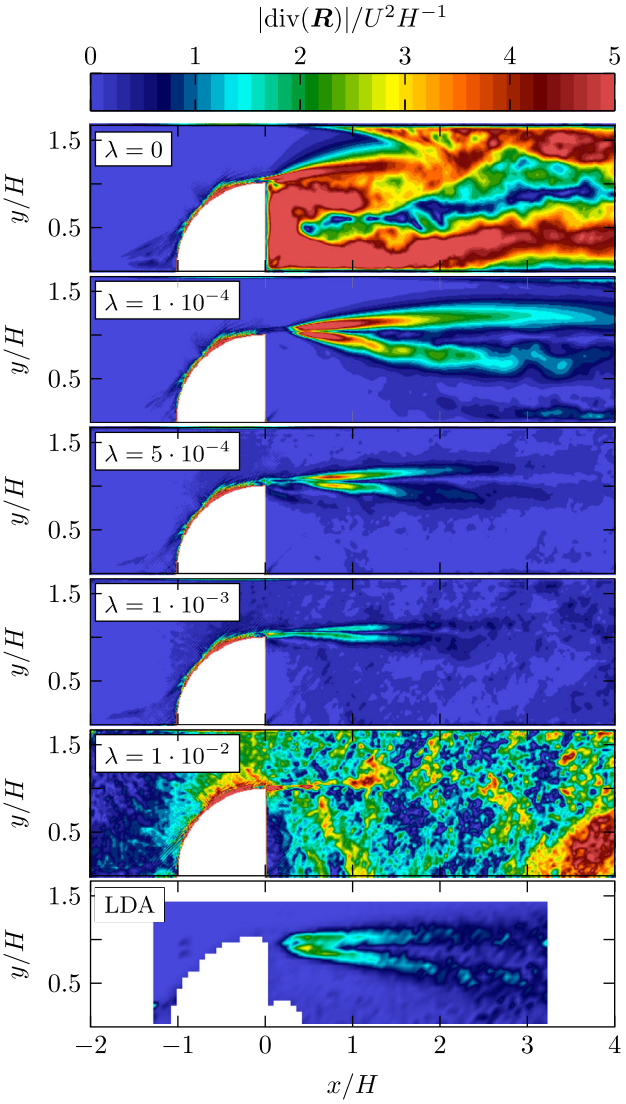

FIGURE 3 Magnitude of the divergence of the Reynolds stress tensor, determined via Equation (10) for the two-dimensional Lattice-Boltzmann simulation (top) and several hybrid datasets (middle) and as measured via LDA (bottom). The scale is identical for all depicted cases. LDA, laser Doppler anemometry

magnitude of the Reynolds stress term drops significantly and higher values are only observed at the edges of the shear layer that originates from the top of the bluff body. Comparing the contour plot of $\lambda = 5 \cdot 10^{-4}$ with the LDA results reveals that it is closest to the measured data, i.e., the LDA measurements are well reproduced, especially when considering that only time-averaged velocity data is introduced into the hybrid simulations. The right-hand side of Equation (10) depends on the gradients of the Reynolds stresses. These stresses do not originate from the molecular viscosity, which is the reason they are not covered by the third term on the left-hand side of Equation (10). In fact, they lie within the shear layer, the position of which is clearly visible in Figure 4, which shows a line-plot of the time-averaged horizontal velocity component at $x/H = 1$. In this figure, the agreement between the hybrid simulation and the experimental data is slightly better for $\lambda = 1 \cdot 10^{-2}$ compared with $\lambda = 5 \cdot 10^{-4}$, despite the fact that in the latter case, the hybrid simulation is able to produce the best results for the divergence of the Reynolds stress tensor. Although the velocity profile for $\lambda = 5 \cdot 10^{-4}$ generally follows the measured MRV points in Figure 4, the deviation overall increases in comparison to $\lambda = 1 \cdot 10^{-2}$. This is especially visible at $y/H \leq 0.8$, where the velocity is slightly overestimated by the hybrid simulation. Nevertheless, with higher values for λ the hybrid simulation is forced to reproduce more and more local fluctuations of the experimental data, which are most likely the result of measurement noise. Therefore, in Figure 3, larger values of the Reynolds stress term appear in small spatial structures all over the flow field for $\lambda = 1 \cdot 10^{-2}$. These nonphysical stresses override the physical turbulent Reynolds stresses in the shear layer which are not clearly visible anymore.

Finally, Figure 5 juxtaposes the contours of the averaged velocity in x-direction in the vicinity of the body in the mid-plane of the unfiltered MRV data and the two-dimensional hybrid simulation results for $\lambda = 5 \cdot 10^{-4}$. It becomes apparent that the hybrid simulation is able to smooth the data while still preserving the general flow features.

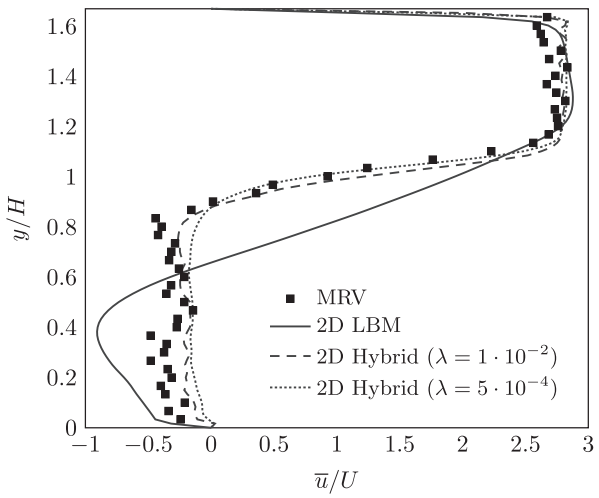

FIGURE 4 Time-averaged horizontal velocity component at $x/H = 1$

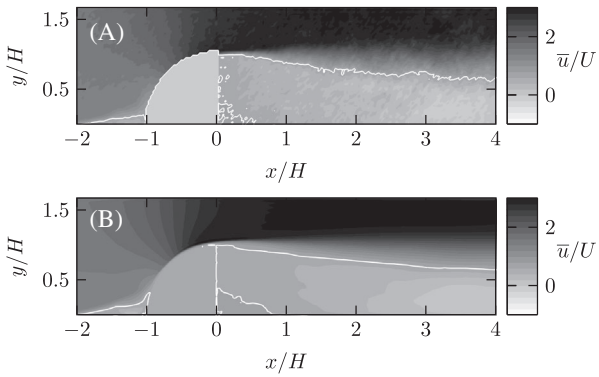

FIGURE 5 Time-averaged horizontal velocity component as measured with A, MRV and B, from a two-dimensional hybrid simulation with $\lambda = 5 \cdot 10^{-4}$. MRV, magnetic resonance velocimetry

Furthermore, the hybrid dataset also provides the pressure and velocity in close proximity to the wall, which becomes especially important when wall shear stresses are of interest.

4 | CONCLUSION

Overall, the proposed approach of incorporating experimental MRV data into LB simulations via the equilibrium term has shown to provide excellent results. The measured velocity is physically smoothed without violating the underlying RANS equations. In two dimensions, an optimal choice of the parameter λ has proven to reproduce the contribution from the Reynolds stress tensor. This is especially of interest considering that only time-averaged velocity data has been incorporated into the simulations. This preliminary study, however, also revealed that there is no resilient method yet to determine which value for λ is best. The determination of an ideal λ is not straightforward and certainly an aspect to consider in more detail in future work. That is, the presented approach offers an ideal basis for further investigations in the direction of hybrid datasets based on LB simulations, eventually enabling a physically based smoothing and correction of any kind of experimental velocity data. Simultaneously, this approach will allow for spatially more extended simulations, which are locally influenced and guided by the incorporated data.

AUTHOR CONTRIBUTIONS

Helen Morrison: Conceptualization-equal; methodology-equal; software-lead; visualization-equal; writing-original draft-lead; writing-review and editing-supporting. **Andreas Lintermann:** Conceptualization-equal; methodology-equal; writing-review and editing-lead. **Sven Grundmann:** Conceptualization-equal; methodology-equal; visualization-equal; writing-original draft-supporting; writing-review and editing-supporting.

PEER REVIEW INFORMATION

Engineering Reports thanks the anonymous reviewers for their contribution to the peer review of this work.

CONFLICT OF INTEREST

The authors declare no potential conflict of interests.

ORCID

Helen E. Morrison https://orcid.org/0000-0002-4444-5883
Andreas Lintermann https://orcid.org/0000-0003-3321-6599
Sven Grundmann https://orcid.org/0000-0003-3116-1918

REFERENCES

1. Evensen G. *Data Assimilation*. Springer: Berlin, Heidelberg/Germany; 2009.
2. Wang B, Zou X, Zhu J. Data assimilation and its applications. *PNAS*. 2000;97(21):11143-11144. https://doi.org/10.1007/s00024-011-0388-x.
3. Blum J, Dimet FXL, Navon IM. Data assimilation for geophysical fluids. In: Temam RM, Tribbia JJ, eds. *Special Volume: Computational Methods for the Atmosphere and the Oceans. 14 of Handbook of Numerical Analysis*. Netherlands: Elsevier; 2009:385-441. https://doi.org/10.1016/S1570-8659(08)00209-3.
4. D'Elia M, Perego M, Veneziani A. A variational data assimilation procedure for the incompressible Navier-Stokes equations in hemodynamics. *J Sci Comput*. 2012;52(2):340-359. https://doi.org/10.1007/s10915-011-9547-6.
5. Suzuki T, Mizushima T, Yamamoto F. Hybrid unsteady flow simulation combining PTV and DNS at moderate reynolds numbers. Paper presented at: Proceeding of the 37th AIAA Fluid Dynamics Conference and Exhibit; June 2007. https://doi.org/10.2514/6.2007-4512.
6. Suzuki T, Yamamoto F. Hierarchy of hybrid unsteady-flow simulations integrating time-resolved PTV with DNS and their data-assimilation capabilities. *Fluid Dyn Res*. 2015;47(5):051407. https://doi.org/10.1088/0169-5983/47/5/051407.
7. Ma X, Karniadakis GE, Park H, Gharib M. DPIV-driven flow simulation: a new computational paradigm. *Proc Royal Soc London Ser A Math Phys Eng Sci*. 2003;459(2031):547-565. https://doi.org/10.1098/rspa.2002.0981.
8. Suzuki T. POD-based reduced-order hybrid simulation using the data-driven transfer function with time-resolved PTV feedback. *Exp Fluids*. 2014;55(8):1798. https://doi.org/10.1007/s00348-014-1798-1.
9. Romain L, Chatellier L, David L. Bayesian inference applied to spatio-temporal reconstruction of flows around a NACA0012 airfoil. *Exp Fluids*. 2014;55(4):1699. https://doi.org/10.1007/s00348-014-1699-3.
10. Suzuki T. Reduced-order Kalman-filtered hybrid simulation combining particle tracking velocimetry and direct numerical simulation. *J Fluid Mech*. 2012;709:249-288. https://doi.org/10.1017/jfm.2012.334.
11. Grundmann S, Wassermann F, Lorenz R, Jung B, Tropea C. Experimental investigation of helical structures in swirling flows. *Int J Heat Fluid Flow*. 2012;37:51-63. https://doi.org/10.1016/j.ijheatfluidflow.2012.05.003.
12. Freudenhammer D, Peterson B, Ding CP, Boehm B, Grundmann S. The influence of cylinder head geometry variations on the volumetric intake flow captured by magnetic resonance velocimetry. *SAE Int J Engines*. 2015;8(4):1826-1836. https://doi.org/10.4271/2015-01-1697.
13. Lintermann A, Schröder W. A hierarchical numerical journey through the nasal cavity: from nose-like models to real anatomies. *Flow, Turbul Combus*. 2019;102(1):89-116. https://doi.org/10.1007/s10494-017-9876-0.
14. Waldmann M, Lintermann A, Choi YJ, Schröder W. Analysis of the effects of MARME treatment on respiratory flow using the Lattice-Boltzmann method. Darmstadt, Germany: Springer. 2020 (pp. 853–863). https://doi.org/10.1007/978-3-030-25253-3_80.
15. Lintermann A, Meinke M, Schröder W. Zonal Flow Solver (ZFS): a highly efficient multi-physics simulation framework. *Int J Comput Fluid Dyn*. 2020;1-28. https://doi.org/10.1080/10618562.2020.1742328.
16. Klemens F, Schuhmann S, Guthausen G, Thäter G, Krause MJ. CFD-MRI: a coupled measurement and simulation approach for accurate fluid flow characterisation and domain identification. *Comput Fluids*. 2018;166:218-224. https://doi.org/10.1016/j.compfluid.2018.02.022.
17. Lemke M, Reiss J, Sesterhenn J. Adjoint based optimisation of reactive compressible flows. *Combust Flame*. 2014;161(10):2552-2564. https://doi.org/10.1016/j.combustflame.2014.03.020.
18. Lemke M, Sesterhenn J. Adjoint-based pressure determination from PIV data in compressible flows validation and assessment based on synthetic data. *Europ J Mech B/Fluids*. 2016;58:29-38. https://doi.org/10.1016/j.euromechflu.2016.03.006.
19. Gray J, Lemke M, Reiss J, Paschereit C, Sesterhenn J, Moeck J. A compact shock-focusing geometry for detonation initiation: Experiments and adjoint-based variational data assimilation. *Combust Flame*. 2017;183:144-156. https://doi.org/10.1016/j.combustflame.2017.03.014.
20. Qian YH, D'Humières D, Lallemand P. Lattice BGK models for Navier-Stokes equation. *Europhy Lett (EPL)*. 1992;17(6):479-484. https://doi.org/10.1209/0295-5075/17/6/001.
21. Bhatnagar PL, Gross EP, Krook M. A model for collision processes in gases. I. small amplitude processes in charged and neutral one-component systems. *Phys Rev*. 1954;94(3):511-525. https://doi.org/10.1103/PhysRev.94.511.
22. Nathen P, Gaudlitz D, Krause MJ, Adams NA. On the stability and accuracy of the BGK, MRT and RLB Boltzmann schemes for the simulation of turbulent flows. *Commun Comput Phys*. 2018;23(3):1-31. https://doi.org/10.4208/cicp.OA-2016-0229.
23. Lallemand P, Luo LS. Theory of the lattice Boltzmann method: dispersion, dissipation, isotropy, Galilean invariance, and stability. *Phys Rev E*. 2000;61(6):6546-6562. https://doi.org/10.1103/PhysRevE.61.6546.

24. Karlin IV, Bösch F, Chikatamarla SS. Gibbs' principle for the lattice-kinetic theory of fluid dynamics. *Phys Rev E*. 2014;90(3):031302. https://doi.org/10.1103/PhysRevE.90.031302.
25. Bösch F, Chikatamarla SS, Karlin IV. Entropic multirelaxation lattice Boltzmann models for turbulent flows. *Phys Rev E*. 2015;92(4):043309. https://doi.org/10.1103/PhysRevE.92.043309.
26. D'Humieres D, Ginzburg I, Krafczyk M, Lallemand P, Luo LS. Multiple-relaxation-time lattice Boltzmann models in three dimensions. *Philos Trans R Soc A Math Phys Eng Sci*. 2002;360(1792):437-451. https://doi.org/10.1098/rsta.2001.0955.
27. Geller S, Uphoff S, Krafczyk M. Turbulent jet computations based on MRT and Cascaded Lattice Boltzmann models. *Comput Math Appl*. 2013;65(12):1956-1966. https://doi.org/10.1016/j.camwa.2013.04.013.
28. Geier M, Greiner A, Korvink JG. Cascaded digital lattice Boltzmann automata for high Reynolds number flow. *Phys Rev E*. 2006;73(6):066705. https://doi.org/10.1103/PhysRevE.73.066705.
29. Ginzburg I. Equilibrium-type and link-type lattice Boltzmann models for generic advection and anisotropic-dispersion equation. *Adv Water Res*. 2005;28(11):1171-1195. https://doi.org/10.1016/j.advwatres.2005.03.004.
30. Latt J, Chopard B. Lattice Boltzmann method with regularized pre-collision distribution functions. *Math Comput Simul*. 2006;72(2-6):165-168. https://doi.org/10.1016/j.matcom.2006.05.017.
31. Geier M, Schönherr M, Pasquali A, Krafczyk M. The cumulant lattice Boltzmann equation in three dimensions: theory and validation. *Comput Math Appl*. 2015;70(4):507-547. https://doi.org/10.1016/j.camwa.2015.05.001.
32. Aidun CK, Clausen JR. Lattice-Boltzmann method for complex flows. *Annu Rev Fluid Mech*. 2010;42(1):439-472. https://doi.org/10.1146/annurev-fluid-121108-145519.
33. Elkins CJ, Alley MT, Saetran L, Eaton JK. Three-dimensional magnetic resonance velocimetry measurements of turbulence quantities in complex flow. *Exp Fluids*. 2009;46(2):285-296. https://doi.org/10.1007/s00348-008-0559-4.
34. Freudenhammer DK. *Magnetic Resonance Velocimetry for Unsteady Flows* (PhD thesis). Technische Universität Darmstadt, Darmstadt; 2017.
35. Chikatamarla S, Karlin I. Entropic lattice Boltzmann method for turbulent flow simulations: Boundary conditions. *Phys A: Stat Mech Appl*. 2013;392(9):1925-1930. https://doi.org/10.1016/j.physa.2012.12.034.
36. Zou Q, He X. On pressure and velocity boundary conditions for the lattice Boltzmann BGK model. *Phys Fluids*. 1997;9:1591-1598. https://doi.org/10.1063/1.869307.
37. Chikatamarla SS, Ansumali S, Karlin IV. Grad's approximation for missing data in lattice Boltzmann simulations. *Europhys Lett*. 2006;74(2):215-221. https://doi.org/10.1209/epl/i2005-10535-x.
38. Bouzidi M, Firdaouss M, Lallemand P. Momentum transfer of a Boltzmann-lattice fluid with boundaries. *Phys Fluids*. 2001;13(11):3452-3459. https://doi.org/10.1063/1.1399290.
39. Morrison HE, Leder A. Sediment transport in turbulent flows with the lattice Boltzmann method. *Comput Fluids*. 2018;172:340-351. https://doi.org/10.1016/j.compfluid.2018.04.015.

How to cite this article: Morrison HE, Lintermann A, Grundmann S. Hybrid datasets: Incorporating experimental data into Lattice-Boltzmann simulations. *Engineering Reports*. 2020;2:e12177. https://doi.org/10.1002/eng2.12177